MJO Initiation Triggered by Amplification of Upper-tropospheric Dry Mixed Rossby-gravity Waves

Daisuke Takasuka[1], Tsubasa Kohyama[2], Hiroaki Miura[3], and Tamaki Suematsu[4]

[1]Japan Agency for Marine-Earth Science and Technology
[2]Ochanomizu University
[3]University of Tokyo
[4]Atmosphere and Ocean Research Institute, The University of Tokyo

November 23, 2022

Abstract

A possibly important dynamical process for the Madden–Julian oscillation (MJO) convective initiation is proposed. An MJO event during the "CINDY2011" field campaign is triggered by eastward-moving lower-tropospheric mixed Rossby-gravity (MRG) wave packets, and its leading precursor is predominance of upper-tropospheric MRGs in the Indian Ocean (IO). Simple three-dimensional model experiments reveal that the upper-tropospheric MRGs in the IO are amplified particularly in the western IO (WIO) by their westward advection and wave accumulation due to the upper-level convergence in mean easterlies of the Walker circulation. The model also predicts downward dispersion of the amplified upper-tropospheric MRGs and resultant lower-tropospheric MRG wave packet formation. This MRG evolution consistently explains the MJO initiation process during CINDY2011, which is further verified by ray tracing for MRGs. Upper-tropospheric circumnavigating Kelvin waves assist the proposed mechanism by promoting MRG-wave accumulation (advection) in their westerly (easterly) phases via enhanced zonal convergence and weakened easterlies (enhanced easterlies).

MJO Initiation Triggered by Amplification of Upper-tropospheric Dry Mixed Rossby–gravity Waves

Daisuke Takasuka[1], Tsubasa Kohyama[2], Hiroaki Miura[3], and Tamaki Suematsu[4]

[1]Japan Agency for Marine-Earth Science and Technology, Yokohama, Japan
[2]Department of Information Sciences, Ochanomizu University, Tokyo, Japan
[3]Department of Earth and Planetary Sciences, The University of Tokyo, Tokyo, Japan
[4]Atmosphere and Ocean Research Institute, The University of Tokyo, Kashiwa, Japan

Key Points:

- Amplification of upper-level MRGs above the western Indian Ocean (WIO) can lead to MJO initiation via low-level MRG-wave packet formation
- Upper-level MRGs propagating into the WIO are amplified by wave accumulation through the mean Walker circulation and then dispersed downward
- Upper-level circumnavigating Kelvin waves can assist MRG-induced MJO initiation by promoting MRG wave accumulation in the WIO

Abstract

A possibly important dynamical process for the Madden–Julian oscillation (MJO) convective initiation is proposed. An MJO event during the "CINDY2011" field campaign is triggered by eastward-moving lower-tropospheric mixed Rossby-gravity (MRG) wave packets, and its leading precursor is predominance of upper-tropospheric MRGs in the Indian Ocean (IO). Simple three-dimensional model experiments reveal that the upper-tropospheric MRGs in the IO are amplified particularly in the western IO (WIO) by their westward advection and wave accumulation due to the upper-level convergence in mean easterlies of the Walker circulation. The model also predicts downward dispersion of the amplified upper-tropospheric MRGs and resultant lower-tropospheric MRG wave packet formation. This MRG evolution consistently explains the MJO initiation process during CINDY2011, which is further verified by ray tracing for MRGs. Upper-tropospheric circumnavigating Kelvin waves assist the proposed mechanism by promoting MRG-wave accumulation (advection) in their westerly (easterly) phases via enhanced zonal convergence and weakened easterlies (enhanced easterlies).

Plain Language Summary

In the tropics, there exists a huge cluster of clouds and rainfall systems moving from the western Indian Ocean (WIO) to the western Pacific, called the Madden–Julian Oscillation (MJO). It is of great interest how and when MJO clouds are formed in the WIO because of their large impacts on global weather patterns, but we have not fully understood it yet. Using a simplified computer simulation and observational data, we find that the formation of MJO tall clouds can start from the "upper-sky" ($\sim$ 10 km altitude) short-period wind variations. During the no-cloud period of MJO, energy of upper-sky wind variations can be input above the central Indian Ocean. Then, it is carried to the WIO and amplified there by upper-sky easterly winds and their convergence associated with the seasonal atmospheric circulation. Because the amplified upper-sky wind energy above the WIO is further dispersed downward, near-surface wind variations become active, which triggers MJO clouds. This new mechanism is theoretically plausible but has been confirmed only in a limited case. It thus should be evaluated for more observations.

1 Introduction

The Madden–Julian oscillation (MJO) is the most prominent intraseasonal variability in the tropics (Madden & Julian, 1972), observed as an eastward-propagating large-scale organized convective system over the Indo-Pacific region. The whole picture of the MJO cannot be explained by classical equatorial wave theories (Matsuno, 1966; Takayabu, 1994; Wheeler & Kiladis, 1999). Also, the MJO has extensive impacts on global weather patterns (Zhang, 2013). It thus has been of great interest to scrutinize the MJO mechanics and to improve the MJO prediction capability over the past decades. In particular, revealing the physics underlying MJO initiation is one of challenging tasks, as inferred from the fact that many pathways to MJO onset in the Indian Ocean (IO) have been proposed (Jiang et al., 2020, and references therein).

MJO initiation processes can be largely divided into two stages; S_1) establishment of large-scale environments favorable for MJO initiation, and S_2) MJO convective outbreaks under the S_1. The S_1 is often explained as "preconditioning" via MJO-scale anomalous horizontal moisture advection (e.g., Kiranmayi & Maloney, 2011; Zhao et al., 2013) and gradual shallow-to-deep pre-moistening called the "discharge-recharge mechanism" (e.g., Bladé & Hartmann, 1993; Benedict & Randall, 2007). Presumably, these processes commonly help MJO convective organization by promoting moisture accumulation.

It is non-trivial when MJO convection is triggered during the preconditioning, however. For instance, Xu and Rutledge (2016) showed that the transition into deep convection is sometimes more rapid than the prediction from the discharge-recharge mechanism. To fill this deficiency in *thermodynamic*-driven processes, we should scrutinize *dynamic* variations as external forcing at the S_2. Specifically, equatorially circumnavigating Kelvin waves (e.g., Seo & Kim, 2003; Powell & Houze, 2015; Chen & Zhang, 2019) and extratropical disturbances (e.g., Hsu et al., 1990; Ray & Zhang, 2010; Gahtan & Roundy, 2019) can trigger MJO convection by inducing upward motions directly, although it is still debated how robust and plausible the proposed processes are.

This paper focuses on the S_2, particularly dynamic roles of mixed Rossby–gravity waves (MRGs) in triggering of MJO convection, which is motivated by several observational studies (Straub & Kiladis, 2003; Yasunaga et al., 2010; D. Yang & Ingersoll, 2011; Takasuka et al., 2019; Takasuka & Satoh, 2020). Field observations clearly detected MRGs enhanced in the mid-to-upper troposphere during the MJO-suppressed phase (Yasunaga et al., 2010; Takasuka et al., 2019), which supports a notion that those MRGs determine the timing of MJO convective outbreaks in the IO through rapid moistening and/or the development of low-level convergence. Moreover, some previous studies showed that eastward group velocity of MRGs assists the start of MJO propagation (D. Yang & Ingersoll, 2011; Takasuka et al., 2019; Takasuka & Satoh, 2020).

The aforementioned findings imply that mid-to-upper-tropospheric MRGs may be sometimes influential precursors of MJO initiation. A question here is how upper-tropospheric MRGs finally initiate MJO convection, which is more likely to be affected by lower-tropospheric moisture fields. Takasuka and Satoh (2020) statistically suggested that upper-tropospheric MRG energy input by more diabatic heating associated with MRG–convection coupling results in downward dispersion of MRGs and the formation of low-level MRG wave packets leading to MJO initiation. However, because upper-tropospheric diabatic heating is rooted in lower-tropospheric moisture/wind variations, diabatic processes may not be a primary trigger for low-level MRGs stemming from the upper troposphere. Hence, it is worth examining whether, as an intrinsic mechanism for MJO initiation in which amplification of upper-tropospheric MRGs is involved, there exists a process more in line with upper-tropospheric dynamics.

In this regard, we shed light on the dry interaction between upper-tropospheric MRGs and a wall-like sharp downward branch (SDB) of the Walker circulation (WC) above the western IO (WIO) (Kohyama et al., 2021). Because SDB climatologically forces upper-tropospheric zonal convergence in easterlies over the IO, MRGs approaching there may be amplified by wave accumulation (Hoskins & Yang, 2016) and then be dispersed downward and eastward. Motivated by this insight, we aim to verify the possibility that dry MRG dynamics can play an essential role in MJO initiation, based on simple model simulations and observational data analyses. A possible role of circumnavigating Kelvin waves in the MJO–MRG relationship is also discussed.

2 Data and Model Descriptions

2.1 Observational Data

To provide observational evidence for our hypothesis, we analyze “MJO2” event initiated in mid-November 2011 during a field campaign CINDY2011 (Yoneyama et al., 2013). We use 3-hourly radiosonde observations at Gan Island (0.7°S, 73.2°E), 6-hourly atmospheric fields from ERA-Interim (Dee et al., 2011) with 27 vertical layers spanning 1000–100 hPa, and 6-hourly rainfall data from the Global Satellite Mapping of Precipitation (GSMaP; Okamoto et al., 2005). A horizontal grid interval of the ERA-Interim (GSMaP) is 0.5° (0.1°). The ERA-Interim data and others covered the entire period of October/November and November 2011, respectively. Note that the boreal-winter (November to March) climatology used in section 4 is derived from the period of 1979–2012.

Anomalies are calculated by subtracting the mean during the data period. To capture MRG variations, we filter 6-hourly anomalies for westward-propagating wavenumbers and periods of 3.5–8 days (cf. section 3), using fast Fourier transforms in space and a 101-point Lanczos filter in time (Duchon, 1979).

2.2 Simple Dry Model

Based on Stechmann et al. (2008), a simple dry model with the barotropic and the first and second baroclinic modes for the vertical depth of $H = 16$ km is constructed on the equatorial β-plane. The model equations are

$$\frac{\partial \zeta_0}{\partial t} + v_0 = -\nabla \times \mathcal{D}_{\mathbf{u}_0}(\mathbf{u}_0, \mathbf{u}_1, \mathbf{u}_2) - \frac{\zeta_0}{\tau_{\mathbf{u}}} + K_{\mathbf{u}} \nabla^4 \zeta_0 \tag{1}$$

$$\frac{\partial \mathbf{u}_j}{\partial t} + y\mathbf{u}_j^{\perp} - \nabla \theta_j = -\mathcal{D}_{\mathbf{u}_j}(\mathbf{u}_0, \mathbf{u}_1, \mathbf{u}_2) - \frac{\mathbf{u}_j}{\tau_{\mathbf{u}}} + K_{\mathbf{u}} \nabla^4 \mathbf{u}_j \quad (\text{for } j = 1, 2) \tag{2}$$

$$\frac{\partial \theta_1}{\partial t} - \nabla \cdot \mathbf{u}_1 = -\mathcal{D}_{\theta_1}(\mathbf{u}_0, \mathbf{u}_1, \mathbf{u}_2, \theta_1, \theta_2) - \frac{\theta_1}{\tau_\theta} + S_{\theta_1} + K_\theta \nabla^4 \theta_1 \tag{3}$$

$$\frac{\partial \theta_2}{\partial t} - \frac{1}{4}\nabla \cdot \mathbf{u}_2 = -\mathcal{D}_{\theta_2}(\mathbf{u}_0, \mathbf{u}_1, \theta_1, \theta_2) - \frac{\theta_2}{\tau_\theta} + S_{\theta_2} + K_\theta \nabla^4 \theta_2 \tag{4}$$

where $\mathbf{u} = (u, v)^T$ is the horizontal wind vector; $\mathbf{u}^{\perp} = (-v, u)^T$; θ is potential temperature; ζ is relative vorticity; $\tau_{\mathbf{u}}$ (τ_θ) is the time scale of damping (cooling) for $\mathbf{u}$ (θ); and S_θ is the heat source. Subscripts j for prognostic variables represent the barotropic ($j = 0$) and first and second baroclinic modes ($j = 1, 2$), and the nonlinear advection terms $\mathcal{D}_{\mathbf{u}_j, \theta_j}$ are given by

$$\mathcal{D}_{\mathbf{u}_0} = \sum_{j=0}^{2} \mathbf{u}_j \cdot \nabla \mathbf{u}_j + \sum_{j=1}^{2} (\nabla \cdot \mathbf{u}_j)\mathbf{u}_j$$

$$\mathcal{D}_{\mathbf{u}_1} = \mathbf{u}_0 \cdot \nabla \mathbf{u}_1 + \mathbf{u}_1 \cdot \nabla \mathbf{u}_0 + \frac{1}{\sqrt{2}}\left[\mathbf{u}_1 \cdot \nabla \mathbf{u}_2 + \mathbf{u}_2 \cdot \nabla \mathbf{u}_1 + 2(\nabla \cdot \mathbf{u}_1)\mathbf{u}_2 + \frac{1}{2}(\nabla \cdot \mathbf{u}_2)\mathbf{u}_1\right]$$

$$\mathcal{D}_{\mathbf{u}_2} = \mathbf{u}_0 \cdot \nabla \mathbf{u}_2 + \mathbf{u}_2 \cdot \nabla \mathbf{u}_0 + \frac{1}{\sqrt{2}}[\mathbf{u}_1 \cdot \nabla \mathbf{u}_1 - (\nabla \cdot \mathbf{u}_1)\mathbf{u}_1]$$

$$\mathcal{D}_{\theta_1} = \mathbf{u}_0 \cdot \nabla \theta_1 + \frac{1}{\sqrt{2}}\left[2\mathbf{u}_1 \cdot \nabla \theta_2 - \mathbf{u}_2 \cdot \nabla \theta_1 + 4(\nabla \cdot \mathbf{u}_1)\theta_2 - \frac{1}{2}(\nabla \cdot \mathbf{u}_2)\theta_1\right]$$

$$\mathcal{D}_{\theta_2} = \mathbf{u}_0 \cdot \nabla \theta_2 + \frac{1}{2\sqrt{2}}[\mathbf{u}_1 \cdot \nabla \theta_1 - (\nabla \cdot \mathbf{u}_1)\theta_1]$$

Equations (1)–(4) start with the three-dimensional Boussinesq system (Majda, 2003), and they have been nondimensionalized by the scaling used in Stechmann et al. (2008). The derivation of (1)–(4) is provided in the supporting information (Text S1).

Solutions to the present model are numerically obtained for specific $S_{\theta_{1,2}}$ distributions and initial conditions given to examine the interaction between WC and MRGs (see section 4.1 for details). We assume a zonally-periodic meridionally-bounded channel of which the zonal and meridional extent is 40,000 km (nearly the circumference along the equator) and 8,000 km, respectively. In all simulations, a grid spacing of 100 km on the Arakawa C-grid and a time step of 15 min for the third-order Runge-Kutta scheme are used. For the fourth-order horizontal diffusion (the damping/cooling) term in (1)–(4), we adopt $K_{\mathbf{u}} = K_\theta = 1.6 \times 10^{14}$ m^4 s^{-1} ($\tau_{\mathbf{u}} = \tau_\theta = 20$ days).

3 Observational Evidence of MRG Variations Leading to MJO initiation

"MJO2" event during CINDY2011, initiated in the WIO around 17 November (see Figs. 1c–e for 10°N–10°S rainfall variations in the time–longitude sections), stems from

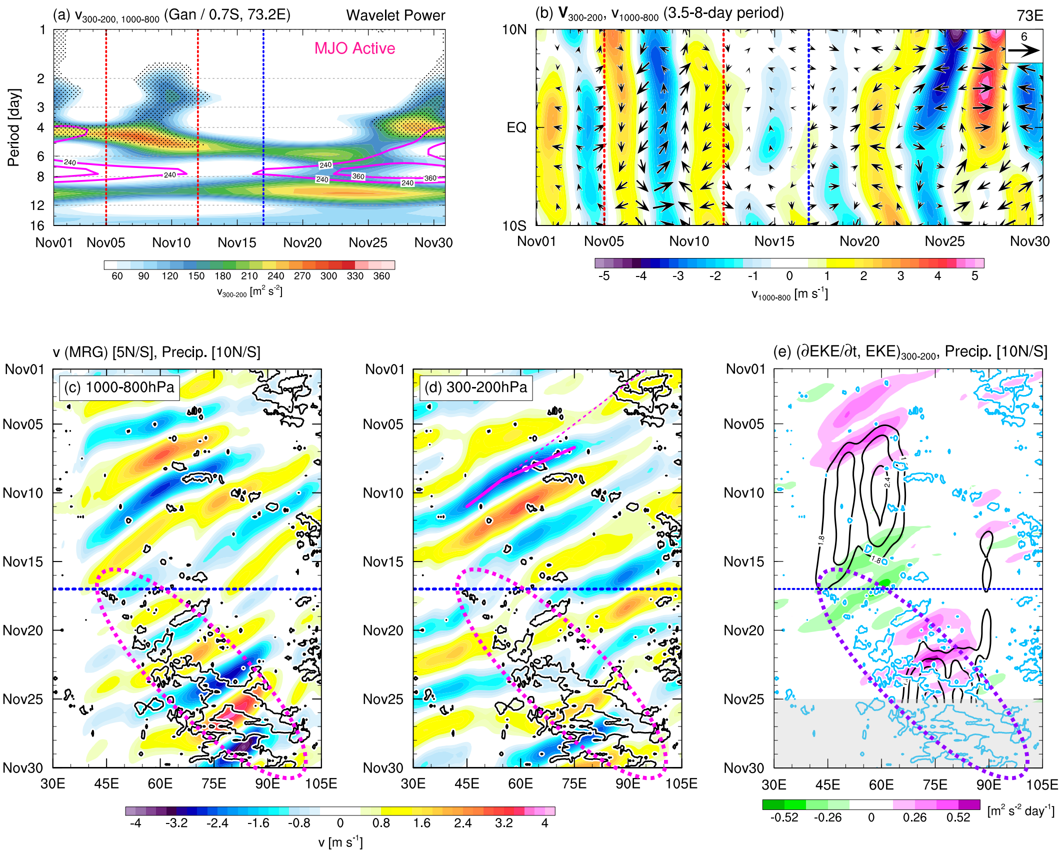

Figure 1. (a) Wavelet power of radiosonde-derived 300–200-hPa and 1000–800-hPa meridional winds (shading and contours) at Gan. Stippling for shading denotes statistical significance at the 95% level. (b) Time-latitude diagram at 73°E of 3.5–8-day bandpass-filtered horizontal winds at 300–200 hPa (vectors) and meridional winds at 1000–800 hPa (shading). (c,d) Time-longitude diagrams of 5°S–5°N averaged MRG-filtered meridional wind anomalies at (c) 1000–800 hPa and (d) 300–200 hPa (shading) and 10°S–10°N averaged precipitation with 0.8 mm/hr (contours). Ellipses indicate MJO2. (e) As in (c,d), but for 10°S–10°N averaged MRG-related EKE at 300–200 hPa (black contours) and its tendency (shading).

amplification of upper-tropospheric MRGs. In Fig. 1a, the wavelet analysis (Torrence & Compo, 1998) for radiosonde-derived meridional winds at Gan highlights significant 4–5.5-day period variations at 300–200 hPa during 5–12 November (shading), after enhanced lower-tropospheric variations in the 6–8-day cycle (contours). These wind variations, detected from a 3.5–8-day-filtered data, are associated with cross-equatorial circulations with equatorially symmetric meridional wind signals (Fig. 1b), indicating the robust MRG structure. This amplification of upper-tropospheric MRGs is followed by re-intensification of lower-tropospheric MRGs in the end of November during the MJO-active phase (Figs. 1a,b).

The aforementioned fact is reinforced by the time–longitude diagrams of equatorial MRG-filtered meridional wind anomalies in the upper/lower troposphere and non-filtered precipitation field (Figs. 1c,d). The eastward propagation of MJO2 precipitation in the IO appears to collocate with the eastward formation of lower-tropospheric MRG wave packets beginning with northerlies in 45°–60°E (Fig. 1c). In fact, low-level MRG convergence successively triggers MJO convection from the WIO (Fig. S1), consistent with the view that MRGs can actively contribute to MJO convective initiation (Takasuka et al., 2019; Takasuka & Satoh, 2020). Before this situation, around 10 November, upper-tropospheric MRG variations begin to strengthen over the WIO in conjunction with the slowdown of their westward propagation (Fig. 1d; magenta lines), which slightly precedes the development of the lower-tropospheric MRG wave packets in 45°–60°E. This evolution is also reconfirmed from the MRG-related eddy kinetic energy (EKE) field, defined by $K' = (u'^2+v'^2)/2$ where primes denote MRG-filtered values; the positive tendency and subsequent accumulation of upper-level EKE is evidently observed over the WIO before MJO2 initiation (Fig. 1e).

4 Mechanism

Based on the analyses in section 3, we raise two questions: Why are upper-tropospheric MRGs amplified in the WIO?; How are low-level MRG wave packets leading to MJO initiation formed? As for the former question, the amplifying upper-tropospheric MRGs with the slowdown of their phase propagation are reminiscent of the interaction with zonally varying background flows (Hoskins & Yang, 2016). Inspired by this idea, we deductively examine the above questions with simple dry model experiments by focusing on a role of WC, which has the wall-like SDB above the WIO (Kohyama et al., 2021). In parallel, we show that the presented mechanism is applicable to the MJO2 event.

4.1 Relationship Between the Walker Circulation and MRGs

First, WC in the model is obtained as the steady-state response to the time-invariant heat source S_{θ_1,θ_2}. Here, S_{θ_1,θ_2} are set so that $\hat{S}_{\theta_j} = \sqrt{2}S_{\theta_j}\sin(jz\pi/H)$ follows the structure of boreal-winter mean apparent heating $\overline{Q_1}$ (Yanai et al., 1973) computed from the ERA-Interim; the formulation for S_{θ_1,θ_2} is provided in Text S2. For example, Fig. 2a compares the equatorial zonal variations of $\hat{S}_{\theta_1}$ at $z = 8$ km and $\overline{Q_1}$ at 400 hPa, where the first baroclinic components is dominant, subtracted from their zonal mean. $\hat{S}_{\theta_1}$ captures both amplitudes and zonal distributions of $\overline{Q_1}$. Similarly, S_{θ_2} is given to match S_{θ_1} variations except for its amplitudes with reference to Q. Yang et al. (2019).

These S_{θ_1,θ_2} produce the realistic WC after the 200 day from the state of rest, as recognized by a comparison of WC for the model and observed boreal-winter mean (Figs. 2b,c); the wall-like SDB and associated upper-tropospheric zonal convergence over the WIO are reproduced. As expected, the same features as climatology are also realized in the 11-day running mean zonal-vertical circulations before MJO2 initiation (during 5–15 November; Fig. 2d), except for stronger zonal convergence than for the climatology (or the model), which will be discussed later.

Under the simulated WC, we examine how upper-tropospheric MRGs as observed before MJO initiation evolve. Referring to observations (Figs. 1d and S4), we set the initial MRG structure as the zonal wavenumber-8 mode confined in $7500 \leq x \leq 9000$ km (i.e., the eastern side of SDB) with maximum amplitudes at the model top. The horizontal structure of MRGs is derived following Aiyyer and Molinari (2003), and its details are provided in Text S2 and Fig. S2. From the initial condition prepared by superimposing the derived MRG field onto the steady state obtained from a 200-day spin-up integration, we run the model for 30 days.

Figure 3a shows the time-longitude diagram of equatorial upper-/lower-tropospheric meridional wind anomalies for the model. The initial MRG given in a limited area immediately excites westward-propagating MRGs in the upper troposphere. These upper-tropospheric MRGs experience wave contraction and deceleration of phase propagation, which occurs in the upper-level background zonal convergence area with easterlies (Fig. 3c). Along with this contraction, upper-tropospheric MRGs are gradually amplified in

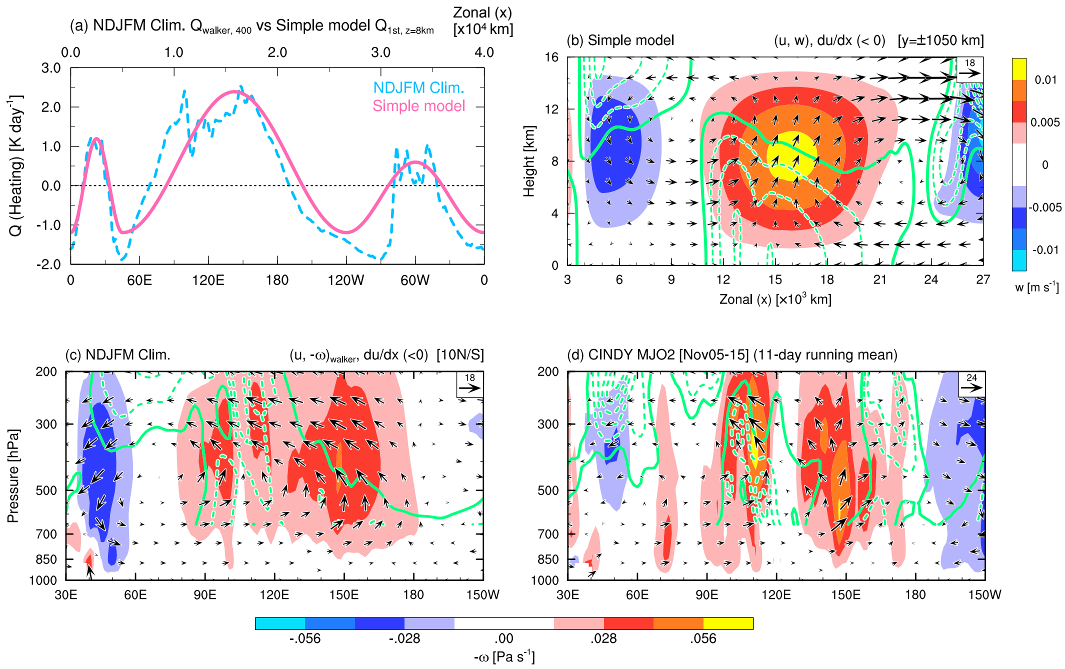

Figure 2. (a) Zonal distributions of $\hat{S}_{\theta_1}$ at $z = 8$ km (pink) and $\overline{Q_1}$ at 400 hPa (blue). (b–d) Zonal-height sections of vertical velocity (shading), zonal-vertical winds (vectors), and zonal convergence (contours) for (b) the spin-up model simulation at day 200, (c) boreal-winter mean, and (d) 11-day running mean fields during 5–15 November. All fields are subtracted from their zonal mean, and averaged over $y = \pm 1050$ km (10°S–10°N) range for the model (observation). Contour interval in (b,d) [(c)] is 1.0 [0.5] $\times$ 10^{-6} /s, with zero contours bolded. Contours below 750 hPa in (c,d) are masked for visibility, and vertical velocity for vectors in (b) and (c,d) is multiplied by 1000 and 400, respectively.

SDB ($4500 \leq x \leq 5500$ km) until around day 15 when they begin to exhibit eastward group velocity, and then lower-tropospheric MRG wave packets are radiated eastward.

In Figs. 3b,d, which are the same as Figs. 3a,c but for the observed MJO2, the processes predicted by the model are similarly detected. After 5 November, upper-tropospheric MRGs propagating westward with small positive group velocity are decelerated and amplified in 45°–60°E, where the zonal convergence associated with SDB is realized. Then, lower-tropospheric MRG wave packets moving eastward are established, which characterizes MJO2 initiation.

Despite much consistency between the model and MJO2, there are some noteworthy differences. One is faster group velocity of the lower-tropospheric MRGs in the model (Figs. 3a,b). This is attributed to the doppler shift by stronger background low-level westerlies (Figs. 3c,d) and deeper equivalent depth in the dry model. The latter reflects the limitation that dry dynamics cannot represent wave–convection coupling effects that are important after MJO initiation.

Another difference is the stronger upper-tropospheric background zonal convergence around SDB before MJO2 initiation (Figs. 3c,d). This is because the observed background WC for MRGs are contributed by not only the climatology but also large-scale circumnavigating Kelvin waves with their evolution slower than MRGs. In fact, upper-tropospheric westerlies associated with circumnavigating Kelvin waves intrude into the WIO (Fig. 3e),

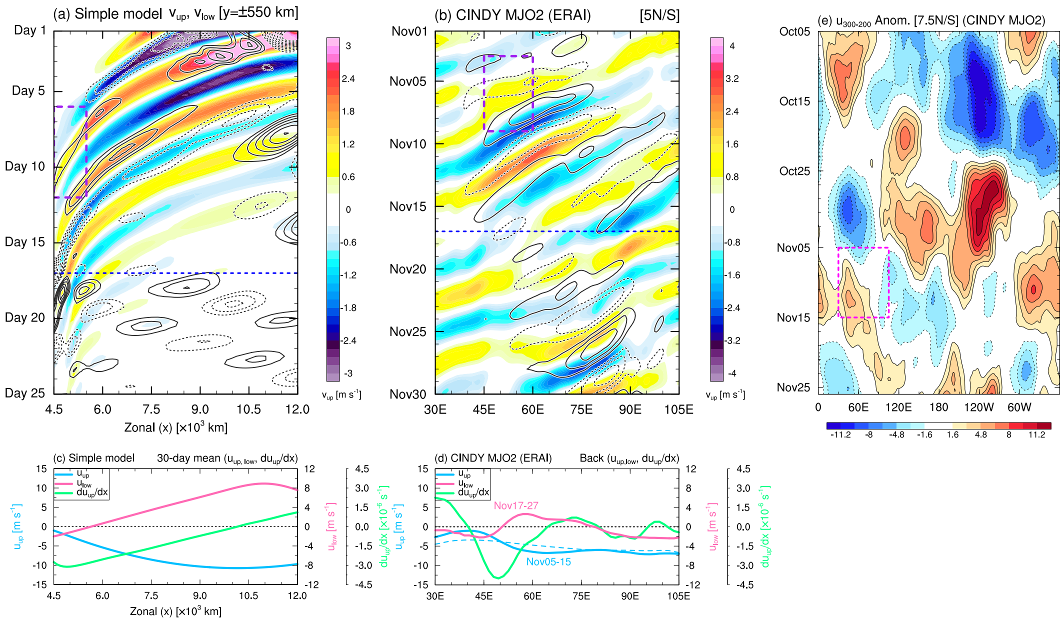

Figure 3. (a,b) Time-longitude diagrams of 24-hr running mean (MRG-filtered) meridional wind anomalies in the upper/lower troposphere (shading/contours) for the model (MJO2). Contours denote ±0.2, ±0.3, ... (±1.0, ± 2.0, ...) m/s with negative values dashed. (c,d) Zonal distributions of upper-/lower-tropospheric zonal winds (blue/pink) and upper-tropospheric zonal convergence (green) for the simulation-period mean in the model (11-day running mean for MJO2). Upper-tropospheric (Lower-tropospheric) fields for MJO2 are computed during 5–15 (17–27) November. Broken lines in (d) denote the boreal-winter mean. (e) Time-longitude diagram of 5-day running mean upper-tropospheric zonal wind anomalies for MJO2. All fields in (a,b) and (c–e) are averaged over $y = \pm$ 550 km (5°S–5°N) and $y = \pm$ 850 km (7.5°S–7.5°N) range for the model (MJO2), respectively. The upper and lower troposphere for the model (MJO2) are defined as the 13.2–16 km and 0–2.8 km (300–200 hPa and 1000–800 hPa) layer, respectively.

which is implied by the stronger background westerlies to the west of 50°E than the boreal-winter mean (Fig. 3d). This process, which is not incorporated in the model, promotes convergence with climatological upper-level easterlies. Considering that zonal convergence can amplify MRGs (see section 4.2), upper-tropospheric circumnavigating Kelvin waves could serve as a catalyst of MRG-induced MJO initiation.

4.2 Amplification of Upper-tropospheric MRGs and Its Impacts on the Lower Troposphere

To reveal why upper-tropospheric MRGs are amplified around SDB and then lower-tropospheric MRG wave packets are formed there, we conduct the EKE budget analysis. The budget equation for the model is

$$\frac{\partial \overline{K'}}{\partial t} = -\underbrace{\overline{\mathbf{u}'(\mathbf{v}'\cdot\nabla)\overline{\mathbf{u}}}}_{K_m K_e} - \underbrace{\overline{\mathbf{v}\cdot\nabla K'}}_{A_m K_e} - \underbrace{\overline{\mathbf{v}'\cdot\nabla K'}}_{A_e K_e} + \underbrace{\overline{w'\theta'}}_{P_e K_e} + \underbrace{\overline{\nabla\cdot(\mathbf{v}'\theta')}}_{GK_e} + (Res.) \tag{5}$$

where $\mathbf{v}$ is the three-dimensional wind vector; w is vertical velocity; and overbars (primes) denote 11-day running mean (deviations from the mean of the 30-day simulation). For the ERA-Interim, primes denote MRG-filtered values, and P_eK_e and GK_e terms are replaced with $-(R/p)\overline{\omega' T'}$ and $-\overline{\nabla\cdot(\mathbf{v}'\Phi')}$, respectively, where ω is vertical p-velocity; T

is temperature; Φ is geopotential; and R is the gas constant. Note that real sources/sinks of EKE are K_mK_e and P_eK_e.

Figures 4a and 4d compare upper-tropospheric EKE budget terms averaged in the time-area domain where MRG amplification occurs for the model and MJO2 (see broken-line squares in Figs. 3a,b). This comparison shows physical consistency with each other; upper-tropospheric MRGs are amplified by EKE advection by background flows (A_mK_e) and the barotropic conversion from the background (K_mK_e). In Figs. 4b,e, the decomposition of these terms,

$$(A_mK_e) = -\overline{u\frac{\partial K'}{\partial x}} - \overline{v\frac{\partial K'}{\partial y}} - \overline{w\frac{\partial K'}{\partial z}} \tag{6}$$

$$(K_mK_e) = -\overline{u'^2\frac{\partial \overline{u}}{\partial x}} - \overline{u'v'\frac{\partial \overline{u}}{\partial y}} - \overline{u'w'\frac{\partial \overline{u}}{\partial z}} - \overline{v'u'\frac{\partial \overline{v}}{\partial x}} - \overline{v'^2\frac{\partial \overline{v}}{\partial y}} - \overline{v'w'\frac{\partial \overline{v}}{\partial z}} \tag{7}$$

reveals that A_mK_e and K_mK_e processes are dominantly contributed by $-\overline{u(\partial K'/\partial x)}$ and $-\overline{u'^2(\partial\overline{u}/\partial x)}$, respectively. This result ensures the following interpretation for upper-tropospheric MRG amplification: upper-level easterlies of WC into SDB efficiently advects MRG energy from the east of SDB, and advected energy is further amplified by wave accumulation due to zonal convergence arising from SDB. Because westward-propagating MRGs (with typical group velocity ~ 5 m/s) are accumulated for their positive ground group velocity in zonal convergence (Hoskins & Yang, 2016), the region near SDB with $\overline{u} > -5$ m/s is indeed appropriate for MRG accumulation (cf. Fig. 3).

Also in the lower-troposphere, the EKE tendency is positive for both the model and MJO2 (Figs. 4c,f), corresponding to the formation of low-level MRG wave packets. For the model (Fig. 4c), this positive tendency almost originates from the EKE redistribution via potential eddy flux convergence (GK_e). Because EKE source here is only upper-tropospheric K_mK_e (Figs. 4a,c), the lower-tropospheric EKE is brought by the energy dispersion from the upper troposphere. Positive lower-tropospheric GK_e with positive upper-tropospheric K_mK_e is also observed for MJO2 (Figs. 4d,f), supporting a notion that process found in the model operates before MJO2 initiation, despite the difference in lower-tropospheric K_mK_e contributions.

The downward impacts of amplification of upper-tropospheric MRGs are qualitatively inferred from the vertically eastward-tilted MRG structure (Fig. S3) and equatorial zonal-height sections of $-\overline{u'^2(\partial\overline{u}/\partial x)}$ and GK_e (Figs. 4g,h). For the model (Fig. 4g), MRG-related EKE is accumulated especially in the inner SDB ($4500 \leq x \leq 5500$ km) in the upper troposphere, and as indicated by positive GK_e below it, the accumulated EKE is redistributed to the mid-to-lower troposphere. This situation reasonably holds true for MJO2 (Fig. 4h), although more EKE redistribution by GK_e is realized to the west of 45°E and around 60°E.

To make the above view more compelling for observation, we conduct 10-day ray tracing of MRGs from around 49°E, 300 hPa ($z \sim 9680$ m), and 10 November, where and when MRG amplification is clearly observed (Figs. S3b and S4). The initial zonal and vertical wavelength (λ_x and λ_z) for ray tracing is roughly estimated as $\lambda_x \sim 47°$ and $\lambda_z \sim 20$ km from the vertical structure (Fig. S3b). For those parameters and $\overline{u} = -5.5$ m/s, the MRG dispersion relation predicts ground zonal phase speed $c_{px} \sim -17$ m/s, consistent with MRGs propagating into the WIO (Fig. S4). Practically, λ_z is difficult to be identified from the vertically-coarse data, so initial λ_z is determined by the MRG dispersion relation with initial λ_x and $c_{px} = -17$ m/s.

This ray tracing reconfirms the downward-eastward energy dispersion of amplified upper-tropospheric MRGs. In Fig. 4h, the rays for 45 initial conditions considering their estimation uncertainties (see Text S3 for method details) indicate that a fraction of rays reach the mid-to-lower troposphere in 50°–70°E after "reflection" in SDB, although others go through SDB westward (as indicated by GK_e distributions).

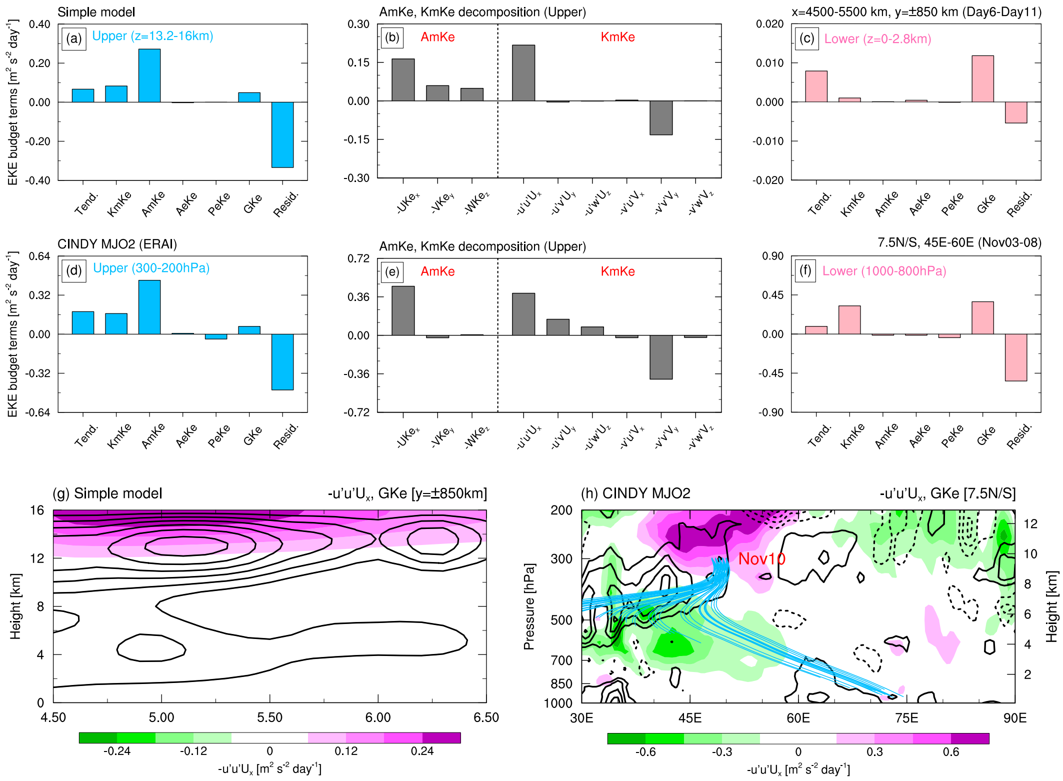

Figure 4. (a,d) All upper-tropospheric EKE budget terms, (b,e) decomposition of upper-tropospheric A_mK_e and K_mK_e, and (c,f) all lower-tropospheric EKE budget terms for the model (top) and MJO2 (bottom). All values are averaged over the time-longitude domain indicated by broken-line squares in Fig. 3a (Fig. 3b) within $y = \pm 850$ km (7.5°S–7.5°N) meridional bands for the model (MJO2). (g,h) Longitude-height sections of $-\overline{u'^2(\partial\overline{u}/\partial x)}$ (shading) and GK_e (contours) for the model (MJO2). Contour interval is 0.015 (0.7) m^2 s^{-2} day $^{-1}$ for the model (MJO2), with negative (zero) values dashed (omitted). Blue lines in (h) denote MRG rays calculated for 45 different initial conditions.

5 Summary and Discussion

In this study, we have presented a new pathway to MJO initiation that stems from dry upper-tropospheric westward-propagating MRGs above the IO. This is inspired by initiation processes of the "MJO2" event during CINDY2011, in which upper-tropospheric MRG amplification in the WIO is followed by MJO2 initiation (Fig. 1). Here we hypothesize that the interaction between MRGs and the Walker circulation (WC) is the key.

To verify our hypothesis, we perform numerical simulations using a simple dry model with three vertical modes, comparing the model output with observations for MJO2. The model captures the essence of the boreal-winter mean WC above the IO: upper-level zonal convergence in mean easterlies blowing into the WIO, where the sharp downward branch (SDB) of WC exists (Figs. 2b,c). In the model with this idealized WC, upper-tropospheric MRGs propagating into SDB are amplified in the inner region of SDB. Then, lower-tropospheric MRG wave packets start to propagate eastward (Figs. 3a,c), resembling the processes of MJO2 initiation triggered by low-level MRG wave packets with eastward group velocity (Figs. 3b,d).

The energetics for this MRG evolution is discussed by both the model experiment and observations (Fig. 4). The initial amplification of upper-tropospheric MRGs in SDB results from MRG energy advection to SDB and wave accumulation due to upper-level easterlies of WC and their zonal convergence arising from SDB. Subsequently, the eastward-downward dispersion of the amplified upper-level MRG energy is activated, which forms lower-tropospheric MRG wave packets leading to MJO initiation.

A difference of WC between the model and MJO2 (Figs. 2b–d) has implication that upper-tropospheric circumnavigating Kelvin waves make the presented mechanism more efficient by modulating background WC additionally. For MJO2, upper-level zonal convergence in SDB are enhanced by cooperation between the westerly phase of Kelvin waves propagating into the WIO and climatological easterlies of WC above the IO (Fig. 3e), which promotes MRG-wave accumulation. In addition, upper-tropospheric Kelvin-wave westerly anomalies help the realization of positive ground group velocity of MRGs by weakening upper-tropospheric mean easterlies, which is advantageous to triggering the wave accumulation (Hoskins & Yang, 2016). Furthermore, the easterly phase of Kelvin waves before the westerly phase can enhance westward advection of MRG energy into the WIO. For these reasons, equatorial circumnavigation of Kelvin waves assists MRG-induced MJO initiation cooperatively with the climatological WC.

The idea proposed in this study for MJO initiation does not require moist processes at all, which provides several debatable topics. First, we may reconsider roles of diabatic processes in the similar MRG-related mechanism suggested by Takasuka et al. (2019) and Takasuka and Satoh (2020). A possible interpretation for this is that dry dynamics are sufficient for an initial trigger of amplification of upper-tropospheric MRGs, although diabatic heating can accelerate and/or maintain MRG amplification in a later stage when MRG–convection coupling becomes evident. Secondly, our idea does not necessarily contradict with the preexisting hypotheses that put emphasis on moisture variations (e.g., Benedict & Randall, 2007; Zhao et al., 2013), because we have tackled MJO initiation in terms of convective triggering by gravity wave dynamics (e.g, Tulich & Mapes, 2008), assuming a favorable environment for organized convection regulated by moisture fields. Nevertheless, if dry MRG dynamics by itself can determine the timing of MJO initiation, it would be misleading to emphasize only the moisture variations for understanding MJO initiation. Because a simple dynamical model theoretically predicts the dry interaction between upper-tropospheric MRGs and WC as observed for a single MJO event, the next step is to examine its robustness and relationship with moist processes statistically for multiple cases.

Acknowledgments

We are grateful to Yukio Masumoto and Tomomichi Ogata for their assistance in our conducting ray tracing. D.T. was supported by JSPS KAKENHI Grant 20J00605, T.K. was supported by JSPS KAKENHI Grants 19K23460 and 20K14554, H.M. was supported by JSPS KAKENHI Grants 16H04048 and 20B202, and T.S. was supported by JSPS KAKENHI Grant 21K13991. The ERA-Interim data are available online (`https://www.ecmwf.int/en/forecasts/datasets/archive-datasets/reanalysis-datasets/era-interim`); GSMaP product is distributed online (`https://sharaku.eorc.jaxa.jp/GSMaP/index.htm`); and radiosonde-derived data during CINDY2011 are archived at `https://data.eol.ucar.edu/dataset/347.008`.

References

Aiyyer, A. R., & Molinari, J. (2003). Evolution of Mixed Rossby–Gravity Waves in Idealized MJO Environments. *Journal of the Atmospheric Sciences*, *60*(23), 2837–2855. doi: 10.1175/1520-0469(2003)060⟨2837:EOMRWI⟩2.0.CO;2

Benedict, J. J., & Randall, D. A. (2007). Observed Characteristics of the MJO Relative to Maximum Rainfall. *Journal of the Atmospheric Sciences*, *64*(7), 2332–2354. doi: 10.1175/JAS3968.1

Bladé, I., & Hartmann, D. L. (1993). Tropical Intraseasonal Oscillations in a Simple Nonlinear Model. *Journal of the Atmospheric Sciences*, *50*(17), 2922–2939. doi: 10.1175/1520-0469(1993)050⟨2922:TIOIAS⟩2.0.CO;2

Chen, X., & Zhang, F. (2019, jan). Relative Roles of Preconditioning Moistening and Global Circumnavigating Mode on the MJO Convective Initiation During DYNAMO. *Geophysical Research Letters*, *46*(2), 1079–1087. doi: 10.1029/2018GL080987

Dee, D. P., Uppala, S. M., Simmons, A. J., Berrisford, P., Poli, P., Kobayashi, S., ... Vitart, F. (2011). The ERA-Interim reanalysis: Configuration and performance of the data assimilation system. *Quarterly Journal of the Royal Meteorological Society*, *137*(656), 553–597. doi: 10.1002/qj.828

Duchon, C. E. (1979, aug). Lanczos Filtering in One and Two Dimensions. *J. Appl. Meteorol.*, *18*(8), 1016–1022. doi: 10.1175/1520-0450(1979)018⟨1016:LFIOAT⟩2.0.CO;2

Gahtan, J., & Roundy, P. (2019). Extratropical Influence on 200-hPa Easterly Acceleration over the Western Indian Ocean Preceding Madden–Julian Oscillation Convective Onset. *Journal of the Atmospheric Sciences*, *76*(1), 265–284. doi: 10.1175/JAS-D-14-0249.1

Hoskins, B. J., & Yang, G.-Y. (2016). The Longitudinal Variation of Equatorial Waves due to Propagation on a Varying Zonal Flow. *Journal of the Atmospheric Sciences*, *2*(1), 605–620. doi: 10.1175/JAS-D-15-0167.1

Hsu, H.-H., Hoskins, B. J., & Jin, F.-F. (1990, apr). The 1985/86 Intraseasonal Oscillation and the Role of the Extratropics. *Journal of the Atmospheric Sciences*, *47*(7), 823–839. doi: 10.1175/1520-0469(1990)047⟨0823:TIOATR⟩2.0.CO;2

Jiang, X., Adames, Á. F., Kim, D., Maloney, E. D., Lin, H., Kim, H., ... Klingaman, N. P. (2020). Fifty years of research on the Madden–Julian Oscillation: Recent progress, challenges, and perspectives. *Journal of Geophysical Research: Atmospheres*, *125*(17), 1–64. doi: 10.1029/2019JD030911

Kiranmayi, L., & Maloney, E. D. (2011). Intraseasonal moist static energy budget in reanalysis data. *Journal of Geophysical Research: Atmospheres*, *116*(21), 1–12. doi: 10.1029/2011JD016031

Kohyama, T., Suematsu, T., Miura, H., & Takasuka, D. (2021). A Wall-like Sharp Downward Branch of the Walker Circulation above the Western Indian Ocean. *ESSOAr*, *1*(1), 1–33. doi: 10.1002/essoar.10505995.1

Madden, R. A., & Julian, P. R. (1972, sep). Description of Global-Scale Circulation Cells in the Tropics with a 40–50 Day Period. *Journal of the Atmospheric Sciences*, *29*(6), 1109–1123. doi: 10.1175/1520-0469(1972)029⟨1109:DOGSCC⟩2.0.CO;2

Majda, A. J. (2003). *Introduction to PDEs and waves in atmosphere and ocean* (1st ed.). Amer Mathematical Society.

Matsuno, T. (1966). Quasi-geostrophic motions in the equatorial area. *Journal of the Meteorological Society of Japan*, *44*(2), 25–43. doi: 10.1002/qj.49710644905

Okamoto, K., Ushio, T., Iguchi, T., Takahashi, N., & Iwanami, K. (2005). The Global Satellite Mapping of Precipitation (GSMaP) project. *International Geoscience and Remote Sensing Symposium (IGARSS)*, *5*(3), 3414–3416. doi: 10.1109/IGARSS.2005.1526575

Powell, S. W., & Houze, R. A. (2015, may). Evolution of precipitation and convective echo top heights observed by TRMM radar over the Indian Ocean during DYNAMO. *Journal of Geophysical Research: Atmospheres*, *120*(9), 3906–3919. doi: 10.1002/2014JD022934

Ray, P., & Zhang, C. (2010). A Case Study of the Mechanics of Extratropical Influence on the Initiation of the Madden–Julian Oscillation. *Journal of the Atmospheric Sciences*, *67*(2), 515–528. doi: 10.1175/2009JAS3059.1

Seo, K.-H., & Kim, K.-Y. (2003). Propagation and initiation mechanisms of the Madden-Julian oscillation. *Journal of Geophysical Research: Atmospheres*, *108*(D13), 4384. doi: 10.1029/2002JD002876

Stechmann, S. N., Majda, A. J., & Khouider, B. (2008). Nonlinear dynamics of hydrostatic internal gravity waves. *Theoretical and Computational Fluid Dynamics*, *22*, 407–432. doi: 10.1007/s00162-008-0080-7

Straub, K. H., & Kiladis, G. N. (2003). Interactions between the Boreal Summer Intraseasonal Oscillation and Higher-Frequency Tropical Wave Activity. *Monthly Weather Review*, *131*(5), 945–960. doi: 10.1175/1520-0493(2003)131⟨0945:IBTBSI⟩2.0.co;2

Takasuka, D., & Satoh, M. (2020). Dynamical Roles of Mixed Rossby–Gravity Waves in Driving Convective Initiation and Propagation of the Madden–Julian Oscillation: General Views. *Journal of the Atmospheric Sciences*, *77*(12), 4211–4231. doi: 10.1175/JAS-D-20-0050.1

Takasuka, D., Satoh, M., & Yokoi, S. (2019, may). Observational Evidence of Mixed Rossby-Gravity Waves as a Driving Force for the MJO Convective Initiation and Propagation. *Geophysical Research Letters*, 2019GL083108. doi: 10.1029/2019GL083108

Takayabu, Y. N. (1994). Large-Scale Cloud Disturbances Features Associated of the with Cloud Equatorial Disturbances Waves. Part I: Spectral Features of the Cloud Disturbances. *Journal of the Meteorological Society of Japan*, *72*(3), 433–449.

Torrence, C., & Compo, G. P. (1998). A Practical Guide to Wavelet Analysis. *Bulletin of the American Meteorological Society*, *79*, 61–78. doi: 10.1175/1520-0477(1998)079⟨0061:APGTWA⟩2.0.CO;2

Tulich, S. N., & Mapes, B. E. (2008). Multiscale convective wave disturbances in the tropics: Insights from a two-dimensional cloud-resolving model. *Journal of the Atmospheric Sciences*, *65*(1), 140–155. doi: 10.1175/2007JAS2353.1

Wheeler, M., & Kiladis, G. N. (1999, feb). Convectively Coupled Equatorial Waves: Analysis of Clouds and Temperature in the Wavenumber–Frequency Domain. *Journal of the Atmospheric Sciences*, *56*(3), 374–399. doi: 10.1175/1520-0469(1999)056⟨0374:CCEWAO⟩2.0.CO;2

Xu, W., & Rutledge, S. A. (2016). Time scales of shallow-to-deep convective transition associated with the onset of Madden-Julian Oscillations. *Geophysical Research Letters*, *43*(6), 2880–2888. doi: 10.1002/2016GL068269

Yanai, M., Esbensen, S., & Chu, J.-H. (1973, may). Determination of Bulk Properties of Tropical Cloud Clusters from Large-Scale Heat and Moisture Budgets. *Journal of the Atmospheric Sciences*, *30*(4), 611–627. doi: 10.1175/1520-0469(1973)030⟨0611:DOBPOT⟩2.0.CO;2

Yang, D., & Ingersoll, A. P. (2011). Testing the Hypothesis that the MJO is a Mixed Rossby–Gravity Wave Packet. *Journal of the Atmospheric Sciences*, *68*(2), 226–239. doi: 10.1175/2010JAS3563.1

Yang, Q., Khouider, B., Majda, A. J., & Chevrotière, D. L. (2019). Northward Propagation, Initiation, and Termination of Boreal Summer Intraseasonal Oscillations in a Zonally Symmetric Model. *Journal of the Atmospheric Sciences*, *76*, 639–668. doi: 10.1175/JAS-D-18-0178.1

Yasunaga, K., Yoneyama, K., Moteki, Q., Fujita, M., Takayabu, Y. N., Suzuki, J., … Mapes, B. (2010). Characteristics of 3–4- and 6–8-Day Period Disturbances Observed over the Tropical Indian Ocean. *Monthly Weather Review*, *138*(11), 4158–4174. doi: 10.1175/2010MWR3469.1

Yoneyama, K., Zhang, C., & Long, C. N. (2013). Tracking pulses of the Madden-Julian oscillation. *Bulletin of the American Meteorological Society*, *94*(12), 1871–1891. doi: 10.1175/BAMS-D-12-00157.1

Zhang, C. (2013). Madden-Julian oscillation: Bridging weather and climate. *Bulletin of the American Meteorological Society*, *94*(12), 1849–1870. doi: 10.1175/BAMS-D-12-00026.1

Zhao, C., Li, T., & Zhou, T. (2013). Precursor signals and processes associated with MJO initiation over the tropical indian ocean. *Journal of Climate*, *26*(1), 291–307. doi: 10.1175/JCLI-D-12-00113.1

Supporting Information for "MJO Initiation Triggered by the Amplification of Upper-tropospheric Dry Mixed Rossby–gravity Waves"

Daisuke Takasuka[1], Tsubasa Kohyama[2], Hiroaki Miura[3], and Tamaki Suematsu[4]

[1]Japan Agency for Marine-Earth Science and Technology, Yokohama, Japan

[2]Department of Information Sciences, Ochanomizu University, Tokyo, Japan

[3]Department of Earth and Planetary Sciences, The University of Tokyo, Tokyo, Japan

[4]Atmosphere and Ocean Research Institute, The University of Tokyo, Kashiwa, Japan

Contents of this file

1. Text S1: Detailed derivation of the simple dry model
2. Text S2: Description of the heat sources and initial MRG structure for the model
3. Text S3: Method of ray tracing for MRGs (Fig. 4h)
4. Figures S1 to S4

Introduction

Text S1 provides derivation of the simple dry model used in the main text (Equations (1)–(4)). In Text S2, we show the formulation of the time-invariant heat sources and initial MRG structure given to the model. Text S3 explains the methodology of ray tracing of MRGs. Figure S1 presents the relationship between low-level MRG convergence and MJO2 initiation in the Indian Ocean, and Figures S2–S4 supplementarily display the structure and evolution of MRGs for the model and MJO2.

Text S1. Detailed derivation of the simple dry model

We here derive the simple dry model utilized in the main text, which starts with the three-dimensional Boussinesq system on the equatorial β-plane (Majda, 2003):

$$\frac{D\mathbf{U}}{Dt} + \beta y \mathbf{U}^{\perp} = -\nabla P + \hat{S}_{\mathbf{U}} \tag{1}$$

$$\nabla \cdot \mathbf{U} + \frac{\partial W}{\partial z} = 0 \tag{2}$$

$$\frac{\partial P}{\partial z} = g\frac{\Theta}{\theta_{\text{ref}}} \tag{3}$$

$$\frac{D\Theta}{Dt} + W\frac{d\overline{\theta}}{dz} = \hat{S}_{\theta} \tag{4}$$

where $\mathbf{U} = (U(x,y,z,t), V(x,y,z,t))^T$ is the horizontal wind vector; $\mathbf{U}^{\perp} = (-V, U)^T$; W is vertical velocity; P is pressure including density; Θ is potential temperature anomalies from the basic state ($= \theta_{\text{ref}} + \overline{\theta}(z)$ where θ_{ref} is constant); g is gravitational acceleration; and $\hat{S}_{\theta}$ and $\hat{S}_{\mathbf{u}}$ is the heat and momentum source, respectively. ∇ is the horizontal gradient operator $(\partial/\partial x, \partial/\partial y)$, and the material derivative (D/Dt) is

$$\frac{D}{Dt} = \frac{\partial}{\partial t} + \mathbf{U}\cdot\nabla + W\frac{\partial}{\partial z}$$

Equations (1)–(4) with dimensions are then nondimensionalized by the scaling introduced in Stechmann, Majda, and Khouider (2008), which leads to the following equations:

$$\frac{D\mathbf{U}}{Dt} + y \mathbf{U}^{\perp} = -\nabla P + \hat{S}_{\mathbf{U}} \tag{5}$$

$$\nabla \cdot \mathbf{U} + \frac{\partial W}{\partial z} = 0 \tag{6}$$

$$\frac{\partial P}{\partial z} = \Theta \tag{7}$$

$$\frac{D\Theta}{Dt} + W = \hat{S}_{\theta} \tag{8}$$

where all variables, forcing, and operators in (5)–(8) have no dimensions.

Imposing the rigid lid conditions at the surface and at the top of the troposphere (i.e., $W = 0$ at $z = 0,\ H$; in nondimensional units, $z = 0,\ \pi$), we expand the variables and sources in (5)–(8) in terms of the vertical eigenmodes (C_j, S_j) as follows:

$$\begin{aligned}
\mathbf{U}(x,y,z,t) &= \sum_{j=0}^{\infty} \mathbf{u}_j(x,y,t)C_j(z), \quad W(x,y,z,t) = \sum_{j=0}^{\infty} w_j(x,y,t)S_j(z) \\
P(x,y,z,t) &= \sum_{j=0}^{\infty} p_j(x,y,t)C_j(z), \quad \Theta(x,y,z,t) = \sum_{j=0}^{\infty} \theta_j(x,y,t)jS_j(z) \\
\hat{S}_{\mathbf{U}}(x,y,z,t) &= \sum_{j=0}^{\infty} S_{\mathbf{u}_j}(x,y,t)C_j(z), \quad \hat{S}_\theta(x,y,z,t) = \sum_{j=0}^{\infty} S_{\theta_j}(x,y,t)S_j(z)
\end{aligned} \tag{9}$$

where the vertical modes C_j, S_j are defined as

$$C_0 = 1, \quad C_j = \sqrt{2}\cos(jz), \quad S_j = \sqrt{2}\sin(jz) \quad (j = 1,2,3...)$$

and for those eigenfunctions, the inner product is defined as

$$\langle F(z), G(z)\rangle = \frac{1}{\pi}\int_0^\pi F(z)G(z)dz$$

For a set of equations (9), we assume that the variables and sources are decomposed by the barotropic mode ($j = 0$) and/or first and second baroclinic modes ($j = 1,2$), because they can capture the main structure of equatorial waves (e.g., Takayabu et al., 1996; Haertel & Kiladis, 2004; Kiladis et al., 2009). That is,

$$\begin{aligned}
\mathbf{U} &= \mathbf{u}_0 + C_1\mathbf{u}_1 + C_2\mathbf{u}_2, \qquad W = w_0 + S_1 w_1 + S_2 w_2 \\
P &= p_0 + C_1 p_1 + C_2 p_2, \qquad \Theta = S_1\theta_1 + 2S_2\theta_2 \\
\hat{S}_{\mathbf{u}} &= S_{\mathbf{u}_0} + C_1 S_{\mathbf{u}_1} + C_2 S_{\mathbf{u}_2}, \quad \hat{S}_\theta = S_1 S_{\theta_1} + S_2 S_{\theta_2}
\end{aligned} \tag{10}$$

Here, the vertical modes for W are restricted by the following arguments. If we substitute the decomposed $\mathbf{U}$ and W into the continuity equation (6) and then compute the inner product with C_0, we obtain

$$\nabla \cdot \mathbf{u}_0 + \frac{\partial w_0}{\partial z} = 0 \tag{11}$$

Integration of (11) from $z' = 0$ to $z' = z$ derives

$$\int_0^z (\nabla \cdot \mathbf{u}_0) dz' + w_0(z) - w_0(0) = 0,$$

so using $w_0(z' = 0) = 0$, we can rewrite this as $w_0(z) = -z(\nabla \cdot \mathbf{u}_0)$. Because the boundary condition $w_0(\pi) = 0$ should be satisfied, $\nabla \cdot \mathbf{u}_0 = 0$ is necessary. Hence, the barotropic mode for W must vanish:

$$w_0 = 0 \tag{12}$$

Under the vertical decomposition in (10) and (12), equations (5)–(8) are projected onto the barotropic and/or first and second baroclinic modes. As an example, we now derive the momentum equation with the barotropic mode. Substitution of (9) into (5) leads to

$$\begin{aligned} \frac{\partial}{\partial t}\left(\sum_{j=0}^{2} C_j \mathbf{u}_j\right) + \sum_{j=0}^{2} C_j \mathbf{u}_j \cdot \nabla \left(\sum_{j=0}^{2} C_j \mathbf{u}_j\right) \ + \ \left(\sum_{j=1}^{2} S_j w_j\right) \frac{\partial}{\partial z}\left(\sum_{j=1}^{2} C_j \mathbf{u}_j\right) + y\left(\sum_{j=0}^{2} C_j \mathbf{u}_j^{\perp}\right) \\ = \ C_1 \nabla \theta_1 + C_2 \nabla \theta_2 + \sum_{j=0}^{2} C_j S_{\mathbf{u}_j} \end{aligned} \tag{13}$$

where $P_j = -\theta_j$ from the hydrostatic equation (7) is used. To extract the barotropic mode from (13), we compute the inner product between (13) and C_0, which derives

$$\frac{\partial \mathbf{u}_0}{\partial t} + \sum_{j=0}^{2} \mathbf{u}_j \cdot \nabla \mathbf{u}_j - \sum_{j=1}^{2} w_j \mathbf{u}_j + y \mathbf{u}_0^{\perp} = S_{\mathbf{u}_0} \tag{14}$$

By applying $w_j = -(1/j)\nabla \cdot \mathbf{u}_j$ from the continuity equation (6) and operating "$\nabla\times$" to (14), we finally obtain the barotropic vorticity (ζ_0) equation:

$$\frac{\partial \zeta_0}{\partial t} + \nabla \times \left[\sum_{j=0}^{2} \mathbf{u}_j \cdot \nabla \mathbf{u}_j + \sum_{j=1}^{2} (\nabla \cdot \mathbf{u}_j) \mathbf{u}_j\right] + v_0 = S_{\zeta_0} \tag{15}$$

where $\zeta_0 = \nabla \times \mathbf{u}_0$, and S_{ζ_0} is the source term for barotropic vorticity. When we adopt $S_{\zeta_0} = -\zeta_0/\tau_{\mathbf{u}}$ and add the diffusion term, the equation (15) corresponds to the equation (1) in the main text. Note that (15) (or (1) in the main text) is numerically solved by predicting a stream function ψ_0, which satisfies the Laplace equation $\zeta_0 = \nabla^2\psi_0$. Following the same procedure as above, we can construct the dry dynamical core completely with equations (1)–(4) in the main text.

Text S2. Description of the heat sources and initial MRG structure for the model

1) Formulations of the time-invariant heat sources

The time-invariant heat sources for the first and second baroclinic modes (S_{θ_1} and S_{θ_2}) are given by

$$S_{\theta_1} = \begin{cases} Q^1_{\theta_1} \cos\left(2\pi \dfrac{x - L_x/16}{L_x/8}\right) \exp(-\beta y^2/c) & \left(0 \le \dfrac{x}{L_x} \le \dfrac{1}{8}\right) \\ (Q^2_{\theta_1} - Q^1_{\theta_1}) + Q^2_{\theta_1} \cos\left[2\pi \dfrac{x - (19/48)L_x}{(13/24)L_x}\right] \exp(-\beta y^2/c) & \left(\dfrac{1}{8} < \dfrac{x}{L_x} < \dfrac{2}{3}\right) \\ (Q^3_{\theta_1} - Q^1_{\theta_1}) + Q^3_{\theta_1} \cos\left[2\pi \dfrac{x - (5/6)L_x}{L_x/3}\right] \exp(-\beta y^2/c) & \left(\dfrac{2}{3} \le \dfrac{x}{L_x} \le 1\right) \end{cases} \quad (16)$$

$$S_{\theta_2} = \begin{cases} Q_{\theta_2} \left|\cos\left(2\pi \dfrac{x - L_x/16}{L_x/8}\right)\right| \exp(-\beta y^2/c) & \left(0 \le \dfrac{x}{L_x} \le \dfrac{1}{8}\right) \\ Q_{\theta_2} \left|\cos\left[2\pi \dfrac{x - (19/48)L_x}{(13/24)L_x}\right]\right| \exp(-\beta y^2/c) & \left(\dfrac{1}{8} < \dfrac{x}{L_x} < \dfrac{2}{3}\right) \\ Q_{\theta_2} \left|\cos\left[2\pi \dfrac{x - (5/6)L_x}{L_x/3}\right]\right| \exp(-\beta y^2/c) & \left(\dfrac{2}{3} \le \dfrac{x}{L_x} \le 1\right) \end{cases} \quad (17)$$

where L_x (= 40,000 km) is the zonal extent of the channel and c (= 50 m/s) is the reference phase speed of gravity waves (Stechmann et al., 2008). Heating amplitudes are set at $(Q^1_{\theta_1},\ Q^2_{\theta_1},\ Q^3_{\theta_1}) = (1.0,\ 1.5,\ 0.75)$ K/day, and $Q_{\theta_2} = 0.226$ K/day. As described in the main text, Q_{θ_2} is the same as that in Yang, Khouider, Majda, and Chevrotière (2019).

2) Formulations of the initial MRG structure

Following Aiyyer and Molinari (2003), we construct the initial MRG structure on the equatorial β-plane. For the first and second baroclinic modes ($j = 1,\ 2$), u_j, v_j, and θ_j associated with MRGs at $t = 0$ are given by

$$\begin{aligned} v_j|_{t=0} &= A_j \phi e^{-\beta y^2/2c} \cos(kx) && (18) \\ u_j|_{t=0} &= A_j \beta y \frac{e^{-\beta y^2/2c}}{k^2c^2 - \omega^2} [(\omega + ck)\phi + 2ck\gamma\phi^*] \sin(kx) && (19) \\ \theta_j|_{t=0} &= -A_j \beta y \overline{\alpha} \frac{e^{-\beta y^2/2c}}{c(k^2c^2 - \omega^2)} [(\omega + ck)\phi + 2\omega\gamma\phi^*] \sin(kx) && (20) \end{aligned}$$

Here, A_j is an arbitrary amplitude factor; k is zonal wavenumber; ω is frequency; $\overline{\alpha} \equiv HN^2\theta_{\mathrm{ref}}/(\pi g)$ is potential temperature scale (N^2 is buoyancy frequency squared; see Stechmann et al. (2008)); and $(\phi, \phi^*; \gamma)$ satisfies the following relation:

$$\phi = {}_1F_1\left(-\frac{\gamma}{2}, \frac{1}{2}, \frac{\beta y^2}{c}\right), \quad \phi^* = {}_1F_1\left(1 - \frac{\gamma}{2}, \frac{3}{2}, \frac{\beta y^2}{c}\right) \tag{21}$$

$$\gamma = \frac{\omega^3 - c^2k\beta - c^2k^2\omega - \beta c\omega}{2\beta c\omega} \tag{22}$$

where ${}_1F_1$ is a Kummer's confluent hypergeometric function. Because $v_j|_{t=0}$ should be vanished at the meridional boundary $y = \pm L_y$ in the equatorial β-channel,

$${}_1F_1\left(-\frac{\gamma}{2}, \frac{1}{2}, \frac{\beta {L_y}^2}{c}\right) = 0 \tag{23}$$

is required from (18) and (21). γ can be numerically obtained from (23), and then a solution of ω in (22) can also be found for given k. As the result, we know all parameters needed to derive the MRG structure from (18)–(20). In this study, the MRG horizontal and vertical structure for $A_1 = -3.0$ and $A_2 = 3.0$ is used, and it is presented in Fig. S2.

Text S3. Method of ray tracing for MRGs (Fig. 4h)

We have conducted ray tracing for MRGs in an equatorial x-z space by integrating the group velocity $\mathbf{C}_g = (C_{gx}, C_{gz})$ and time derivative of the wavenumber vector $\mathbf{k} = (k_x, k_z)$, which are represented by

$$\frac{d_g\mathbf{X}}{dt} \equiv \mathbf{C}_g \tag{24}$$

$$\frac{d_g\mathbf{k}}{dt} \equiv \frac{\partial \mathbf{k}}{\partial t} + \mathbf{C}_g \cdot \nabla \mathbf{k} = -\nabla \Omega \tag{25}$$

where $\mathbf{X} = (X, Z)$ is the position of a ray; and Ω is the dispersion relation of MRGs. When a varying zonal flow $\overline{u}(x, z)$ exists, Ω and $\mathbf{C}_g \equiv (\partial\Omega/\partial k_x, \partial\Omega/\partial k_z)$ are given by

$$\Omega \equiv \omega_i + k_x\overline{u} = \frac{c_e}{2}\left(k - \sqrt{k^2 + 4\beta/c_e}\right) + k_x\overline{u} \tag{26}$$

$$C_{gx} = \frac{c_e}{2}\left(1 - \frac{k_x}{\sqrt{k_x^2 + 4\beta/c_e}}\right) + \overline{u} \tag{27}$$

$$C_{gz} = \mp\frac{\omega_i^3}{N(k_x\omega_i + 2\beta)} \tag{28}$$

where ω_i is intrinsic frequency; $c_e = N/|k_z|$; and N is buoyancy frequency. Although the direction of the vertical phase propagation of MRGs can be both upward and downward, we assumed upward phase propagation (i.e., $k_z < 0$ for $k_x > 0$ and $\omega_i < 0$) because of the eastward-tilted vertical structure (Fig. S3b). Thus, the minus sign is taken in (27), which corresponds to the downward energy dispersion for $\omega_i < 0$. If initial k_x and k_z are given, we can obtain $\mathbf{C}_g$ uniquely using (26)–(28) and start the time integration of (24) and (25) from an arbitrary initial position $\mathbf{X}_{init}$. Subsequently, $\mathbf{k}$, $\mathbf{C}_g$, and $\mathbf{X}$ is updated in turn. We use the fourth-order Runge-Kutta scheme with a time step of 30 min. Background fields ($\overline{u}$ and N) are calculated by linear and spline interpolation of the 6-hourly ERA-Interim data (7.5°S–7.5°N) in space and time, respectively.

As described in the main text (Section 4.2), the initial ray position $\mathbf{X}_{init}$ is around 49°E, 300 hPa ($\sim$ 9680 m), and the initial zonal wavelength λ_x ($= 2\pi/k_x$) is set to be about 47° (see Figs. S3b and S4). Meanwhile, this estimation should include some uncertainties, so we prepare for 45 initial conditions with slight perturbations for $\mathbf{X}_{init}$ and λ_x. Specifically, we have tried combinations of 5 zonal positions (X_{init} = 48°, 48.5°, 49°, 49.5°, 50°), 3 vertical positions (Z_{init} = 9630, 9680, 9730 m), and 3 zonal wavelengths (λ_x = 46°, 47°, 48°). For each λ_x and $c_{px} = -17.0$ m/s (Fig. S4), k_z is determined by the MRG dispersion relation (26) as

$$|k_z| = N \frac{\beta/k_x^2 + c_{px}^i}{(c_{px}^i)^2} \tag{29}$$

where $c_{px}^i = \omega_i/k_x$ ($= c_{px} - \overline{u}$) is the intrinsic zonal phase speed. Consequently, initial λ_z is calculated as λ_z = 19.1, 21.4, and 25.8 km for λ_x = 46°, 47°, and 48°, respectively.

References

Aiyyer, A. R., & Molinari, J. (2003). Evolution of Mixed Rossby–Gravity Waves in Idealized MJO Environments. *J. Atmos. Sci.*, *60*(23), 2837–2855. doi: 10.1175/1520-0469(2003)060⟨2837:EOMRWI⟩2.0.CO;2

Haertel, P. T., & Kiladis, G. N. (2004). Dynamics of 2-Day Equatorial Waves. *J. Atmos. Sci.*, *61*(22), 2707–2721. doi: 10.1175/JAS3352.1

Kiladis, G. N., Wheeler, M. C., Haertel, P. T., Straub, K. H., & Roundy, P. E. (2009). Convectively coupled equatorial waves. *Rev. Geophys.*, *47*(2), RG2003. doi: 10.1029/2008RG000266

Majda, A. J. (2003). *Introduction to PDEs and waves in atmosphere and ocean* (1st ed.). Amer Mathematical Society.

Stechmann, S. N., Majda, A. J., & Khouider, B. (2008). Nonlinear dynamics of hydrostatic internal gravity waves. *Theor. Comput. Fluid Dyn.*, *22*, 407–432. doi: 10.1007/s00162-008-0080-7

Takayabu, Y. N., Lau, K.-M., & Sui, C.-H. (1996). Observation of a Quasi-2-Day Wave during TOGA COARE. *Mon. Wea. Rev.*, *124*(9), 1892–1913.

Yang, Q., Khouider, B., Majda, A. J., & Chevrotière, D. L. (2019). Northward Propagation, Initiation, and Termination of Boreal Summer Intraseasonal Oscillations in a Zonally Symmetric Model. *Journal of the Atmospheric Sciences*, *76*, 639–668. doi: 10.1175/JAS-D-18-0178.1

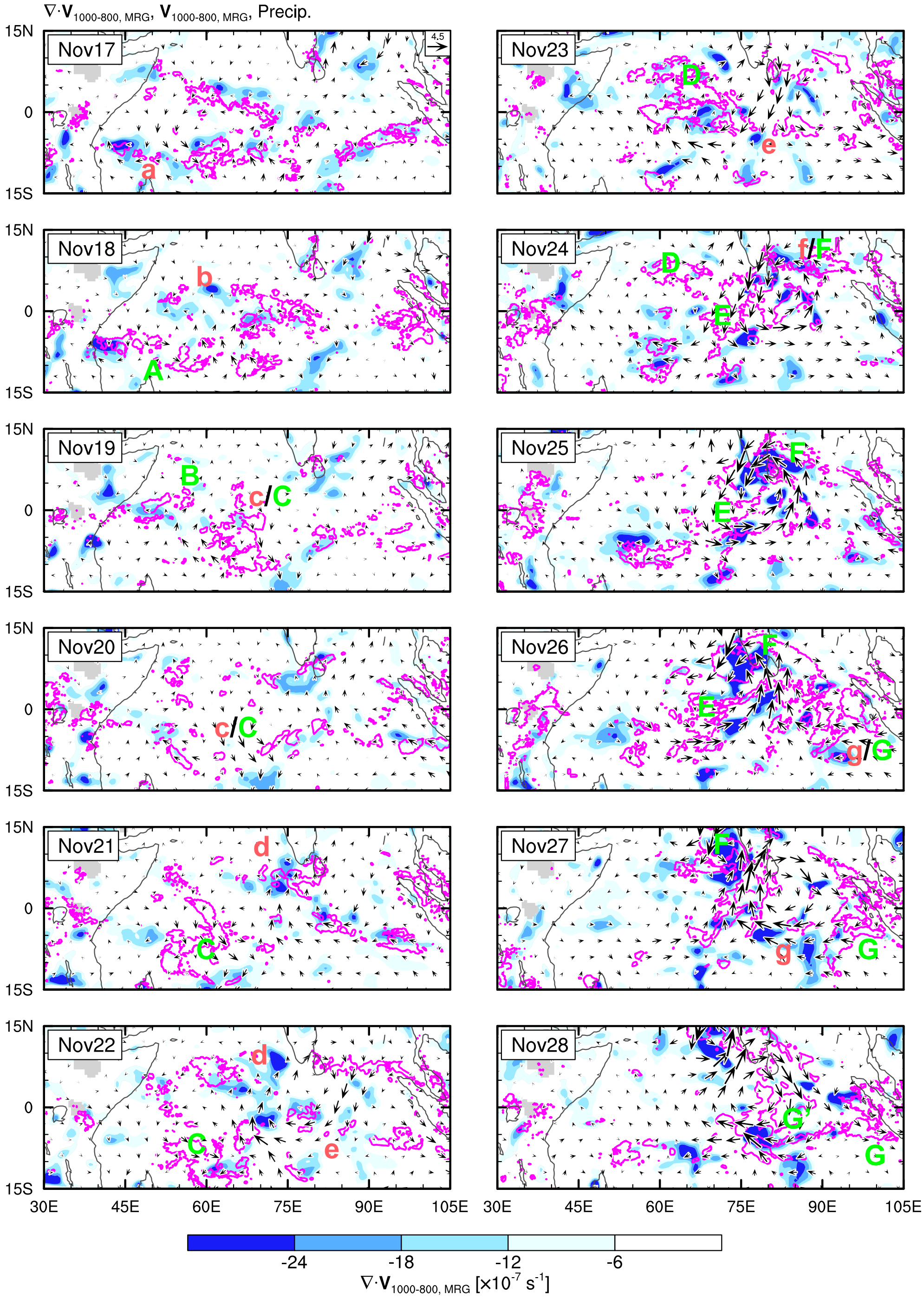

Figure S1. Horizontal maps of MRG-filtered horizontal convergence (shading) and wind anomalies (vectors) at 1000–800 hPa and precipitation (contours with 0.75 mm/hr) from 00UTC 17 to 28 November. Letters a–g and A–G′ denote representative convergence/cross-equatorial flows and corresponding precipitation, respectively (e.g., Convergence "a" is related to precipitation "A", associated with MJO initiation around 17 November).

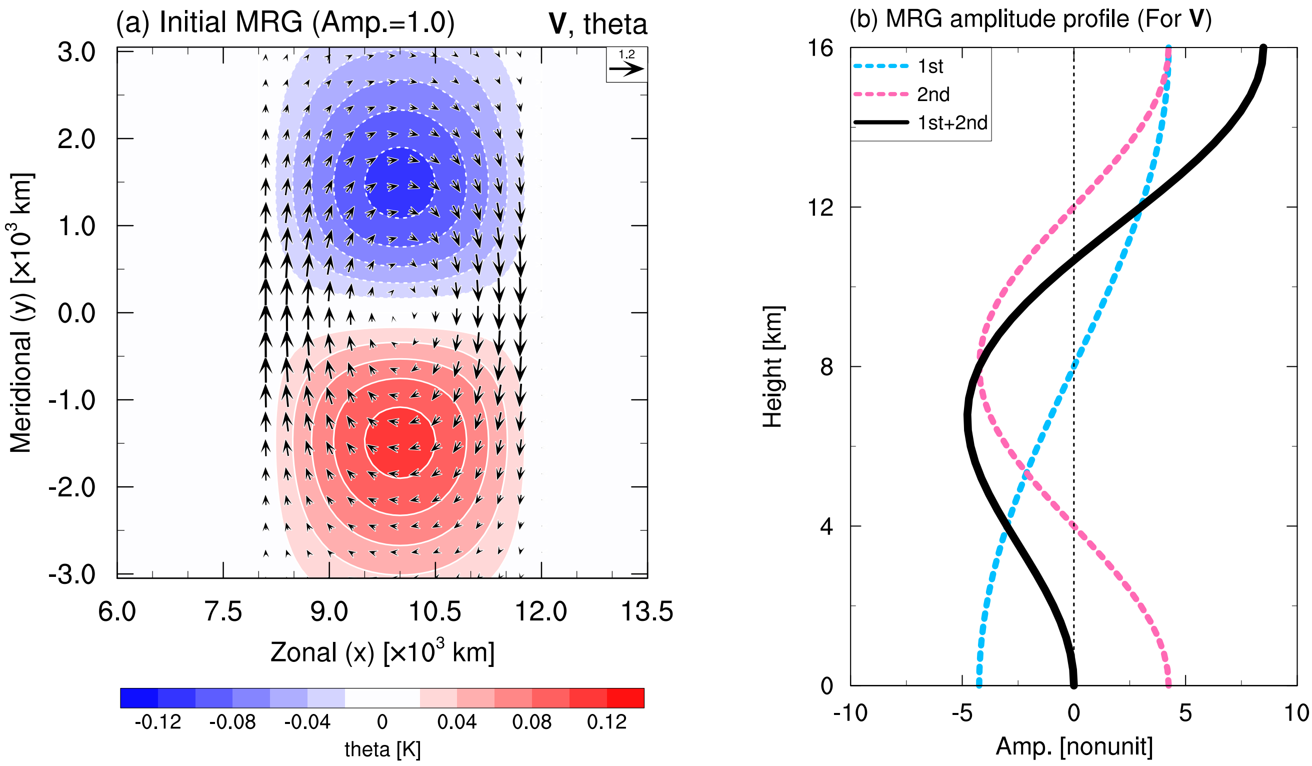

Figure S2. (a) Horizontal map of potential temperature (shading) and wind (vectors) anomalies given as the initial MRG structure for an MRG amplitude factor 1.0. (b) Vertical profile of an MRG amplitude factor for the first and second baroclinic modes (blue and pink) and their superposition (black).

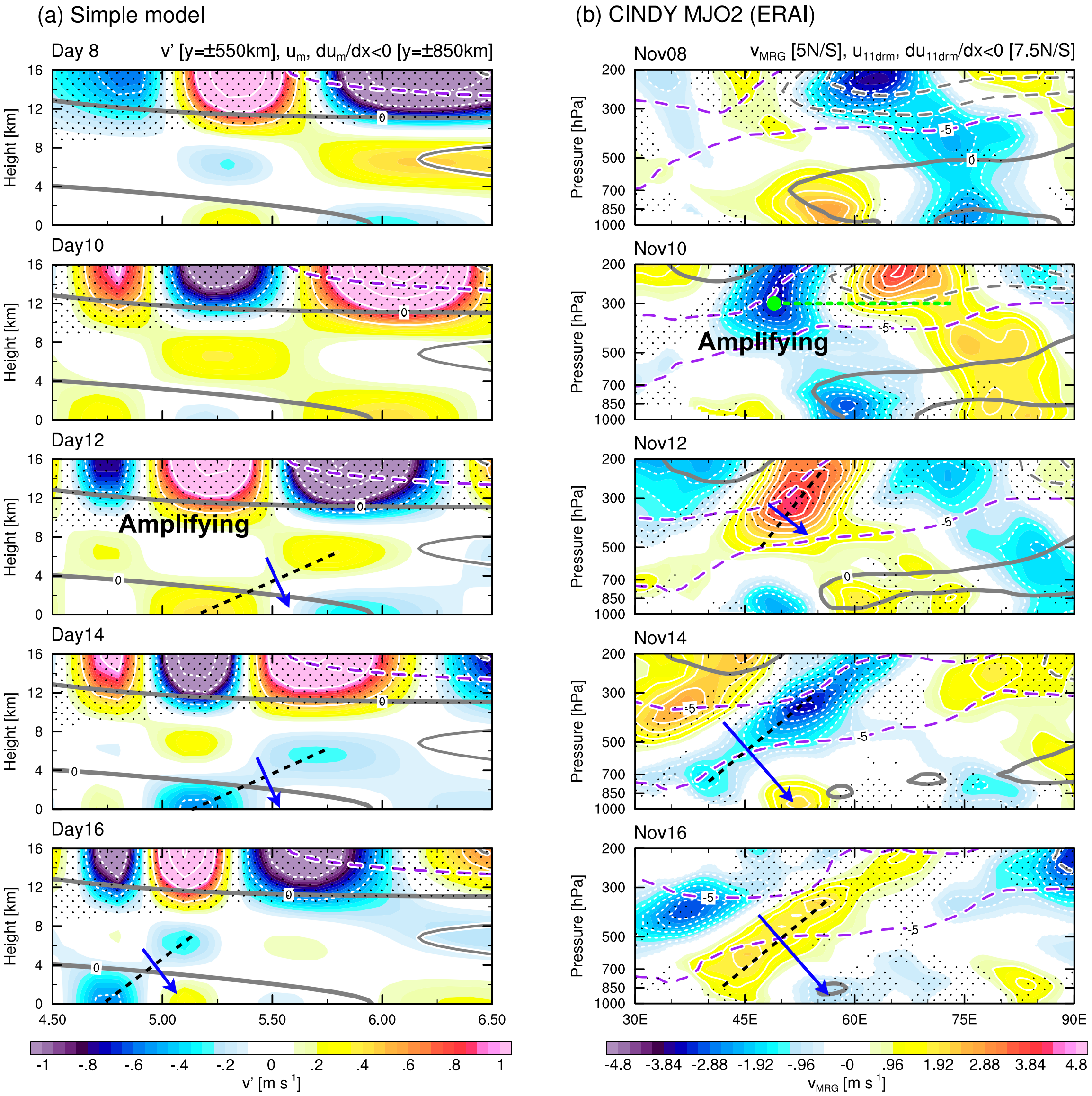

Figure S3. Zonal-height sections of equatorial MRG-related meridional wind anomalies (shading and white contours), background zonal winds (gray and purple contours), and background zonal convergence (stippling) every 2 day for (a) the model from days 8 to 16 and (b) MJO2 from 8 to 16 November. Definitions of anomalies and background fields follow those in Fig. 3. White contour interval is 0.5 (0.48) m/s for the model (MJO2). Gray/purple contour interval is 2.5 m/s from ±5 m/s (purple; −5 m/s), with negative (zero) values broken (bolded). Black-dashed lines and blue arrows represent the eastward-tilted phase lines and expected direction of MRG energy dispersion, respectively. Filled marker on 10 November in (b) denotes $\mathbf{X}_{init}$ for ray tracing.

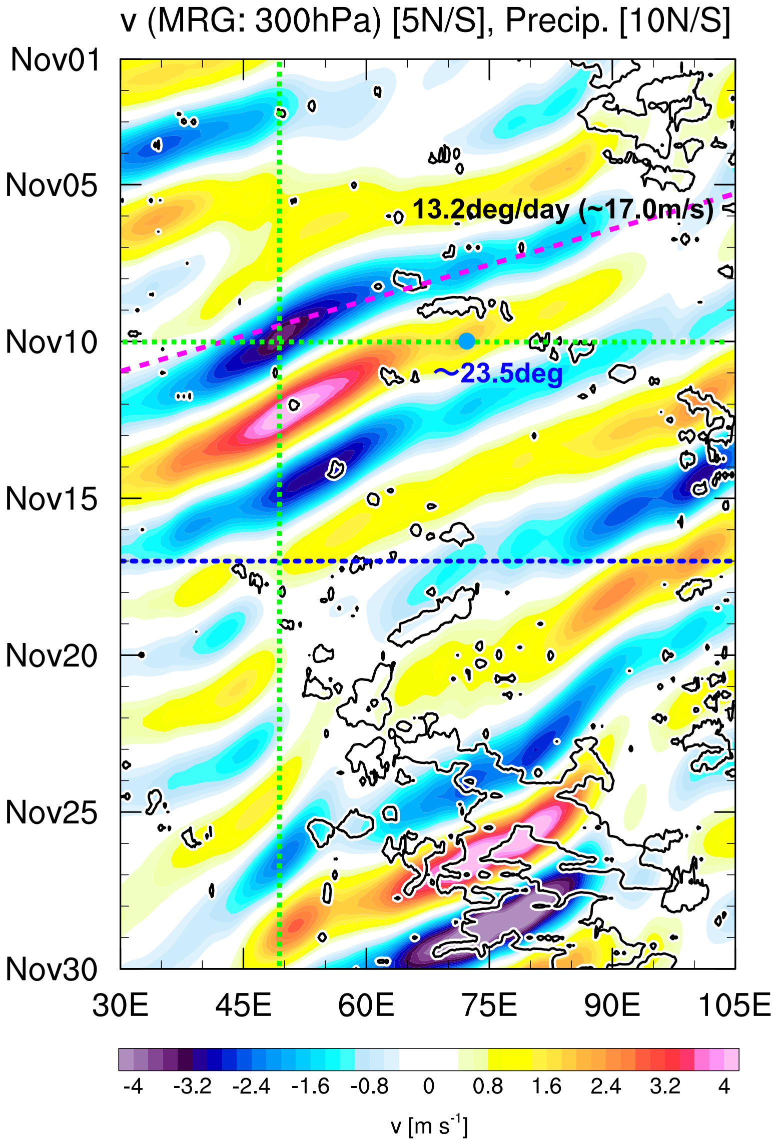

Figure S4. As in Fig. 1d, but for 300 hPa.